INORGANIC CHEMISTRY FRONTIERS

RESEARCH ARTICLE

View Article Online
View Journal | View Issue

Cite this: *Inorg. Chem. Front.*, 2025, **12**, 8690

Highly active superoxide dismutase mimic: pyridine carboxamide-based copper(II) complexes

Róbert Diószegi,[a] Andrea Guidetti,[b] Norbert Ág,[c] Ilenia Serra,[b,d] Dóra Szalóki,[e] Dóra Bonczidai-Kelemen,[a] Nóra V. May,[f] Erzsébet Fekete,[c] Levente Karaffa,[c] István Fábián,[a,e] Sabine Van Doorslaer *[b] and Norbert Lihi *[a,e]

Pyridine-based ligands functionalized with one (PyHis) or two histidine (PydiHis) moieties were synthesized, and their copper(II) complexes were studied as novel antioxidant systems. The complexes were characterized by pH-potentiometric, spectroscopic (UV-vis, circular dichroism, continuous-wave and pulsed electron paramagnetic spectroscopy (EPR)), computational (DFT) and X-ray diffraction methods. The complexes show high thermodynamic stability. The PyHis complex possesses a (COO^-,N_{py},N^-,N_{Im}) donor set, while PydiHis binds copper(II) *via* a (N_{Im},N_{py},N^-,N_{Im}) donor set at physiological pH. The PyHis and PydiHis complexes of copper(II) exhibit negligible (IC_{50} = 147 ± 15 μM) and outstanding (IC_{50} = 0.64 ± 0.07 μM) superoxide dismutase (SOD) activity, respectively. The noted difference is attributed to the structural flexibility of the latter complex as confirmed by pulsed EPR spectroscopy. The antioxidant activity of the copper(II) complexes was also tested *in vivo* by monitoring their effects on the mycelial growth of *Aspergillus niger* under oxidative stress. Both complexes were able to protect the cells under these conditions; however, the copper(II) complex of PydiHis was more effective in accordance with its excellent SOD activity. Consequently, the copper(II) complex of PydiHis stands out as an efficient, low-molecular-weight SOD mimic combining high catalytic activity with proven biological efficacy under oxidative stress conditions, making it a promising candidate for medical applications.

Received 10th August 2025,
Accepted 28th September 2025

DOI: 10.1039/d5qi01687h

rsc.li/frontiers-inorganic

Introduction

The superoxide anion radical, $O_2^{\bullet-}$, is formed during the partial reduction of molecular oxygen in biological systems. The term reactive oxygen species (ROS) refers to $O_2^{\bullet-}$ and further intermediates such as H_2O_2 and $HO^{\bullet}$. A significant amount of molecular oxygen is metabolized into ROS during cellular respiration, and these intermediates act not only as toxic molecules but also as signal species or harmless products.[1,2]

In biological systems, the primary role of antioxidant enzymes is to control the concentration level of ROS and to protect the cells against oxidative damage. Superoxide dismutase enzymes (SODs) are involved in the transformation of $O_2^{\bullet-}$ into molecular oxygen and hydrogen peroxide.[3] These metalloenzymes contain redox-active metal ions in the active center, which facilitate electron transfer during the dismutation cycle of $O_2^{\bullet-}$.[4] Copper, iron, manganese and nickel are the redox-active metal ions in the active center of SOD enzymes; however, zinc(II) plays also an essential role in copper-containing SODs. The rate of SOD-catalyzed disproportionation of $O_2^{\bullet-}$ often approaches the diffusion-controlled limit. Under physiological conditions, the SODs maintain the concentration of $O_2^{\bullet-}$ at a low level (approximately 2×10^{-10} M).[5] The dismutation process is very efficient and the redox reaction does not require any extra energy from the cell.[6] At a reduced concentration level of SOD enzymes, the drastic increase in the concentration of ROS may lead to oxidative stress and cause DNA damage, inflammatory diseases or the development of human cancer.[7,8] Furthermore, several neurodegenerative disorders are associated with elevated ROS concentrations.[9]

Low-molecular-weight transition-metal complexes are capable of assisting the decomposition of $O_2^{\bullet-}$; thus, they can

[a]*Department of Inorganic and Analytical Chemistry, University of Debrecen, H-4032 DebrecenEgyetem tér 1., Hungary. E-mail: lihi.norbert@science.unideb.hu*
[b]*Department of Chemistry, TSM² lab, University of Antwerp, Universiteitsplein 1, 2610 Antwerp, Belgium. E-mail: sabine.vandoorslaer@uantwerpen.be*
[c]*Department of Biochemical Engineering, University of Debrecen, H-4032 DebrecenEgyetem tér 1., Hungary*
[d]*Laboratory of Bioenergetics and Protein Engineering, CNRS/AMU, Marseille, France*
[e]*HUN-REN–UD Mechanisms of Complex Homogeneous and Heterogeneous Chemical Reactions Research Group, University of Debrecen, H-4032 DebrecenEgyetem tér 1., Hungary*
[f]*Centre for Structural Science, Research Centre for Natural Sciences, Hungarian Research Network (HUN-REN), Magyar tudósok körútja 2, H-1117 Budapest, Hungary*

be applied as potential medicines in the treatment of diseases related to an elevated ROS level or used as antiaging agents.[10,11] Since the direct administration of SODs for such purposes is not feasible due to their large size and limited cell permeability, considerable efforts have been focused on developing SOD mimics to overcome some of these limitations.

Recently, we have demonstrated that copper(II) complexes of pyridine-2,6-dicarboxamide ligands are efficient catalysts for the degradation of superoxides.[12] The best result was obtained with the complex of the tyrosine-functionalized ligand (*N*,*N*-pyridine-2,6-dicarbonyl-bis(L-tyrosine)). The excellent SOD activity was determined by considering the interaction between the superoxide anion and the hydroxyl group of tyrosine, which promotes the binding of the superoxide anion to the metal center and enhances the proton transfer in the dismutation cycle. Earlier studies have also shown that positively charged substituents (cationic Mn(III) porphyrins,[13] cationic polyarginine peptides[14] or transition-metal complexes with positively charged quaternary ammonium functions[15]) of the SOD mimics facilitate the electrostatic interaction with the superoxide anion and increase the SOD activity of the complexes. An in-depth investigation of the characteristics of complexes formed with more dedicated ligands is essential to understand how the structure and composition of the ligands modulate the catalytic activity of SOD mimics.

In this paper, we report a comprehensive study on the SOD activity of copper(II) complexes formed with pyridine–carboxamide ligands containing histidine residues (Scheme 1). In the case of PyHis, a histidine moiety may provide a (3N,O) donor set for binding copper(II), while PydiHis may act as a pentadentate ligand with five available nitrogen atoms. The methyl ester of the latter ligand has been previously considered as an anti-HIV metal chelator.[16] The acid–base equilibria and the complex formation processes were fully described by the pH-potentiometric method and further corroborated by several spectroscopic and structural characterization methods, including continuous-wave (CW) and pulsed electron paramagnetic resonance (EPR) spectroscopy and X-ray diffraction (XRD). The SOD activity of the complexes was measured in stopped-flow experiments and by the xanthine/xanthine oxidase/NBT assay. The antioxidant activity of the complexes was also studied *in vivo* by monitoring its effect on the mycelial growth of *Aspergillus niger* NRRL 2270, a robust industrial fungus.

Materials and methods

Materials

Pyridine-2,6-dicarboxylic acid, thionyl chloride, and nitro blue tetrazolium chloride (NBT) were obtained from Merck Millipore and L-histidine was obtained from Alfa Aesar. Methanol, dichloromethane, triethylamine, acetonitrile, and trifluoroacetic acid were obtained from VWR and dioxane was obtained from Reanal, while xanthine and xanthine oxidase were purchased from Sigma-Aldrich. The Cu(II) stock solution was prepared from $CuCl_2{\cdot}2H_2O$ (VWR) using doubly deionized and ultrafiltered water (ELGA Purelab Classic system), and its concentration was determined gravimetrically by precipitation with an oxinate. All reagents were of the highest available purity.

Syntheses

The ligands were prepared using the same procedures as in our previous work (Scheme S1).[12]

L-Histidine methyl ester dihydrochloride (1). The compound was prepared according to a method described in the literature.[17]

***N*,*N*-Pyridine-2,6-dicarbonyl-bis(L-histidine methyl ester) (2).** A mixture of pyridine-2,6-dicarboxylic acid (1.74 g; 10.4 mmol) and thionyl chloride (5.2 ml) in 20 mL of dioxane was refluxed for 1 hour. The excess solvent was removed under reduced pressure to give a brown oil. The obtained pyridine-2,6-dicarbonyl chloride was dissolved in 25 mL of dichloromethane. To a cold (0–5 °C) mixture of **1** (4.76 g; 19.7 mmol) and triethylamine (10 mL) in 150 mL of dichloromethane, pyridine-2,6-dicarbonyl chloride in dichloromethane was added dropwise for 2 hours and stirred at room temperature overnight. The formed solid, triethylamine hydrochloride, was removed with filtration, and the organic solution was washed with 8 × 30 mL of water and dried over magnesium sulfate, and the excess solvent was removed under reduced pressure to obtain solid **2** (1.40 g; 30% yield). ^{1}H NMR (400 MHz, DMSO-d_6): 3.1 (dd, J = 8.5, 6.1 Hz, 2H, CH_2), 3.2 (dd, J = 9.2, 5.6 Hz, 2H, CH_2), 3.7 (s, 6H, CH_3), 4.7 (q, J = 7.8, 5.6 Hz, 2H, CH), 6.9 (s, 2H, histidine–CH), 7.6 (s, 2H, histidine–CH), 8.2 (s, 3H, pyridine–CH), 9.5 (d, J = 7.0 Hz, 2H, NH).

***N*-Pyridine-2-carbonyl-L-histidine (compound 3, PyHis) and *N*,*N*-pyridine-2,6-dicarbonyl-bis(L-histidine) (compound 4,**

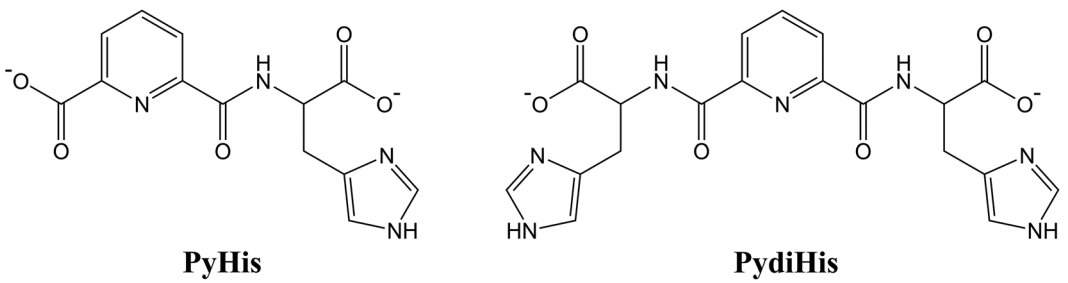

Scheme 1 Structural formulae of the deprotonated form of ligands.

PydiHis). Compound **2** (1.40 g; 3.0 mmol) in 20 mL of 3 M hydrochloric acid was refluxed for exactly 1 hour. The excess solvent was removed by lyophilization. The crude product was purified by preparative HPLC using water and acetonitrile each containing 5 mM trifluoroacetic acid to obtain **3** (0.32 g; 36% yield) and **4** (0.41 g; 31% yield).

PyHis: ^{1}H NMR (400 MHz, DMSO-d_6): 3.2 (dd, J = 9.4, 5.7 Hz, 1H, CH_2), 3.4 (dd, J = 10.5, 4.8 Hz, 1H, CH_2), 4.9 (td, J = 5.0, 4.1 Hz, 1H, CH), 7.4 (s, 1H, histidine–CH), 8.2–8.3 (m, 3H, pyridine–CH), 9.0 (s, 1H, histidine–CH), 9.4 (d, J = 8.6 Hz, 2H, NH). ^{13}C NMR (360 MHz, DMSO-d_6): 26.5 (CH_2), 51.6 (CH), 117.0 (histidine–CH), 125.5 (pyridine–CH), 127.1 (pyridine–CH), 129.7 (histidine–C), 134.0 (histidine–CH_2), 139.9 (pyridine–CH), 146.5 (pyridine–C), 148.8 (pyridine–C), 163.2 (C═O), 165.0 (C═O), 171.8 (C═O). Calcd for $[C_{13}H_{13}N_4O_5]^+$ ($[M + H]^+$): m/z 305.0880. Found: m/z 305.0879 (Fig. S1–S3).

PydiHis: ^{1}H NMR (400 MHz, DMSO-d_6): 3.4 (dd, J = 10.2, 4.9 Hz, 2H, CH_2), 3.5 (dd, J = 10.1, 4.9 Hz, 2H, CH_2), 4.8 (td, J = 5.0, 4.0 Hz, 2H, CH), 7.4 (s, 2H, histidine–CH), 8.2 (s, 3H, pyridine–CH), 8.8 (s, 2H, histidine–CH), 9.8 (d, J = 8.4 Hz, 2H, NH). ^{13}C NMR (360 MHz, DMSO-d_6): 25.8 (CH_2), 52.0 (CH), 117.0 (histidine–CH), 124.9 (pyridine–CH), 130.4 (histidine–C), 133.6 (histidine–CH_2), 139.6 (pyridine–CH), 148.4 (pyridine–C), 163.5 (C═O), 171.9 (C═O). Calcd for $[C_{19}H_{20}N_7O_6]^+$ ($[M + H]^+$): m/z 442.1470. Found: m/z 442.1470. Calcd for $[C_{19}H_{21}N_7O_6]^{2+}$ ($[M + 2H]^{2+}$): m/z 221.5771. Found: m/z 221.5769 (Fig. S4–S6).

Equilibrium studies

The acid dissociation constants (pK_a) of the ligands and the overall stability constants ($\log\beta_{pqr}$) of the copper(II) complexes were determined by pH potentiometric titration using carbonate-free KOH solution (*ca.* 0.2 M) as a titrant at 0.2 M (KCl) ionic strength and 25.0 °C. The Gran method was used to determine the carbonate contamination of the stock solutions.[18] To avoid the interference of the dissolved oxygen and/or carbon dioxide, argon gas was bubbled through the samples during the titrations. The pH values were recorded using a computer-controlled Metrohm 785 DMP Titrino automatic titrator equipped with a Metrohm 6.0234.100 combination glass electrode. The pH values were converted to hydrogen ion concentrations according to the method proposed by Irving *et al.*[19] The PSEQUAD program was used to calculate the acid dissociation constants of the ligands and the overall stability constants of the metal complexes, $\beta_{pqr} = [M_pL_qH_r]/[M]^p[L]^q[H]^r$.[20] Metal ion to ligand ratios were selected between 1 : 2 and 1 : 1. The distribution curves of the metal complexes were calculated using a designated program, MEDUSA.[21]

UV-visible and circular dichroism (CD) spectroscopy

Agilent Technologies Cary 60 and 8454 spectrophotometers were used to record the UV-visible spectra of the copper(II) complexes in the 250–800 nm wavelength range. The concentrations of the samples were the same as in the pH potentiometric titrations. CD spectra were recorded with a Jasco J-810 spectropolarimeter in the 200–800 nm wavelength range using 1 mm or 1 cm cells.

NMR spectroscopy

The pH-dependent ^{1}H NMR spectra of the ligands were recorded using a Bruker Avance 400 spectrometer. 11 individual samples were prepared by dissolving the ligand in H_2O (8 mM) and adjusting the pH to within the range of 1.80–8.50. A capillary containing sodium 3-(trimethylsilyl)-1-propane sulfonate (TSP) in D_2O was immersed in the sample as an external standard for ^{1}H (δ_{TSP} = 0.00 ppm). The water proton signal was suppressed using a Watergate 3–9–19 pulse sequence with gradients.

Electron paramagnetic resonance (EPR) spectroscopy

X-band CW-EPR spectra were recorded using a Bruker ELEXSYS E500 spectrometer (microwave frequency: 9.4 GHz, microwave power: 13 mW, modulation amplitude: 0.5 mT, modulation frequency: 100 kHz) in capillaries averaging 4 scans at room temperature. All spectra were corrected with the background spectrum of pure water. Frozen solution CW-EPR spectra were recorded using quartz EPR tubes that were submerged in liquid nitrogen at 77 K. 0.2 mL aliquots of the samples were introduced into the quartz EPR tubes and 0.05 mL of methanol was added to prevent the crystallization of water. Isotropic CW-EPR spectra were simulated using the "2d_epr" software.[22] Each component curve was characterized by the isotropic EPR parameters (g_o, A_o^{Cu} copper and a_o^N nitrogen hyperfine coupling constants) and relaxation parameters α, β, and γ. The linewidth is given as $\sigma_{M_I} = \alpha + \beta M_I + \gamma M_I^2$, where M_I denotes the magnetic quantum number of the copper nucleus. The frozen solution EPR spectra were simulated using the software created by Rockenbauer and Korecz.[23] The anisotropic spectra were analysed individually by considering the rhombic or axial g- and A-tensors (I_{Cu} = 3/2). When it was possible, nitrogen splittings were described by a_x^N, a_y^N and a_z^N where x, y, and z denote the components of the g-tensor. Since natural $CuCl_2$ was used for the measurements, the spectra were calculated as the sum of the spectra of ^{63}Cu and ^{65}Cu weighted by their natural isotope abundances.

Pulsed EPR experiments were performed using a Bruker ELEXSYS E580 X-band spectrometer (operating at a microwave (mw) frequency of ~9.7 GHz) equipped with a ColdEdge cryogen-free Stinger system and the temperature was set to 5 K. In all experiments, a shot repetition time of 2.5 ms was taken. For field-swept ESE (electron spin echo)-detected EPR measurements, a Hahn echo sequence $\pi/2$–τ–π–τ–echo with 2-step phase cycling was used. A $\pi/2(\pi)$ pulse length of 16 (32) ns was chosen and the spectra are shown as a sum of 256 τ-values starting at 96 ns in steps of 8 ns. HYSCORE (hyperfine sublevel correlation) spectroscopy[24] was performed using the mw pulse sequence $\pi/2$–τ–$\pi/2$–t_1–π–t_2–$\pi/2$–τ–echo with $t_{\pi/2(\pi)}$ = 16(32) ns and t_1 and t_2 varied from 96 to 7280 ns in steps of 16 ns. The τ-values are given in the figure captions. Mims ENDOR[25] (electron nuclear double resonance) spectra were recorded using a mw pulse sequence $\pi/2$–τ–$\pi/2$–T–$\pi/2$–τ–echo

with $t_{\pi/2}$ = 16 ns and T = 20 μs, and a radiofrequency π pulse of length 15 μs during time T. Davies ENDOR[26] experiments were performed using the π–T–π/2–τ–π–τ–echo with $t_{\pi/2(\pi)}$ = 48(96) ns, τ = 400 ns and T = 20 μs, and a radiofrequency π pulse of length 15 μs during time T. Simulations of the pulsed EPR spectra were performed using the EasySpin software[27] implemented in MATLAB (v.6.0.0-dev.51).

Mass spectrometry

ESI-TOF-MS spectra were recorded using a Bruker maXis II MicroTOF-Q type Qq-TOF-MS instrument (Bruker Daltonik, Bremen, Germany) in negative mode. Electrospray ionization was used as an ion source, and a spray voltage of 4 kV was applied. As a drying gas, nitrogen was employed, and the drying temperature was 200 °C. A sampling rate of 2 GHz was used to accumulate and record the spectra. External calibration was applied for the mass spectra using exact masses of sodium formate clusters. The spectra were evaluated using DataAnalysis 4.4 software from Bruker.

SC-XRD experiment

Blue crystals of the copper(II) PyHis complex, $[Cu(PyHisH_{-1})(H_2O)_2Na(H_2O)_4]$, were obtained from an aqueous solution (*ca.* 2 mM). In this crystallization experiment, 600 μL aliquots of the sample were prepared by mixing aqueous $CuCl_2$ solution and the ligand. The pH of the solution was set to 7.0 by adding NaOH solution, and crystallization was induced by subsequent slow evaporation at room temperature. Crystals suitable for XRD analysis weighed only a few milligrams (*ca.* 1–2 mg). However, 2–3 different crystals were analyzed by XRD, which confirmed the integrity of the compound. The crystal was mounted on a loop and transferred to the goniometer. X-ray diffraction data were collected at 143(2) K using a Rigaku RAXIS-RAPID II diffractometer with Mo-Kα radiation. Numerical absorption correction[28] was carried out using the program CrystalClear.[29] The Sir2019[30] program was used to solve the structure and the SHELX program package[31] in WinGX software[32] was used for refinement of the structure, which was done by full-matrix least squares optimization on F^2. Refinement of non-hydrogen atoms was carried out with anisotropic temperature factors. Hydrogen atoms were placed into geometric positions. They were included in structure factor calculations, but they were not refined. The isotropic displacement parameters of the hydrogen atoms were approximated from the U(eq.) value of the atom they were bonded to. The unusual angles between the coordinated water molecules around the Na^+ (O9–Na1–O10 102(2)° and O9–Na1–O8 83.22 (9)°) caused alert levels A and B in IUCr checkcif. However, the deviation from the 90° angle can be interpreted based on the H-bonds formed with neighboring molecules. Selected bond lengths and angles of compounds were calculated using PLATON software.[33] The graphical representation and the editing of CIF files were done using Mercury[34] and enCIFer[35] software. The crystal structure has been deposited as CCDC 2424617.

Cyclic voltammetry (CV)

CV measurements were carried out using a BASI Epsilon Eclipse potentiostat (Bioanalytical Systems Inc., West Lafayette, USA) using a three-electrode arrangement consisting of a platinum wire auxiliary electrode, a glassy carbon working electrode and an Ag/AgCl/3 M KCl reference electrode (all from ALS Co. Japan). The measurements were performed in 0.2 M KNO_3 at 25 °C. An aqueous solution of $K_3[Fe(CN)_6]$ was used to calibrate the system. The samples were degassed before the measurements using argon. The concentration of the samples was 2 mM and the pH was adjusted to 7.6 by the addition of KOH solution. For the CV measurements, the voltage range was varied between −600 and +800 mV at sweep rate of 200 mV s^{-1}.

SOD activity measurements

To determine the SOD activity of the metal complexes, the xanthine/xanthine oxidase/NBT assay was used.[36] In this case, $O_2^{\bullet-}$ is generated by the xanthine/xanthine oxidase system. The radical reacts with *para*-nitro blue tetrazolium chloride (NBT) to produce diformazan and the formation of this compound is followed by UV-vis spectroscopy at 560 nm (25 °C). The addition of the SOD mimic to this system opens up a competitive reaction for the consumption of $O_2^{\bullet-}$ and the production of diformazan becomes slower. This assay was performed at pH 7.6 in phosphate buffer (*ca.* 0.05 M) containing NBT (4.5×10^{-5} M) and xanthine (2×10^{-4} M). The addition of an appropriate amount of xanthine oxidase initiated the reaction, which was associated with an absorbance change of around 0.020–0.025 min^{-1} at 560 nm. First, the reaction was followed in the absence of the Cu(II) complex for 4 minutes; then, the complex was added to the same sample and the absorbance change was monitored for another 4 minutes. The corresponding rates were estimated by fitting each of the two experimental datasets to a straight line. The SOD activity of the copper(II) complex was expressed as the half maximal inhibitory concentration, IC_{50}, and converted to k_{McCF} using the following expression: $k_{McCF} = k_{NBT}[NBT]/IC_{50}$.[37,38]

The decomposition of $O_2^{\bullet-}$ was also studied by the sequential stopped-flow method by monitoring the absorbance decay at 260 nm using an Applied Photophysics SX20-MV stopped-flow instrument as described previously at 25 °C.[39] The measurements were carried out in 1 : 1 aqueous HEPES buffer (50 mM, pH 7.6)/DMSO mixture, and the instrument was used in sequential mode to circumvent artefacts due to the slow homogenization of the reaction mixture when the reactants dissolved in pure water and DMSO were mixed. The kinetic traces were collected as an average of at least 5 runs. The experimental data were evaluated using OriginPro 9.1.[40]

Density functional theory (DFT) computations

Spin-unrestricted DFT computations were performed with the ORCA 5.0 package to calculate the structures of Cu(II) complexes formed with PyHis and PydiHis (*cf.* SI).[41,42] To mimic the solvation effect of water, the conductor-like polarizable continuum model (CPCM) was applied. For geometry optimization of the

Cu(II) complexes, the Becke–Perdew density functional (BP86) was used.[43–45] The Ahlrichs split-valence plus polarization (SVP) basis set was used for all atoms except copper.[46] The Ahlrich (2df,2pd) polarization functions were obtained from the TurboMole basis set library as implemented in ORCA. For the copper atoms, the doubly polarized triple-zeta (TZVPP) (Ahlrichs) basis set was used. The energy was converged to 1×10^{-8} Hartree (Eh) and the tolerances of convergence in the geometry optimization were 3×10^{-4} Eh per Bohr for the gradient and 5×10^{-6} Eh for the total energy. To verify the validity of the obtained geometry, the vibrational frequencies were computed to check that all frequencies were real. For the single-point calculations of the EPR parameters of the Cu(II) complexes, different combinations of density functionals and basis sets were investigated. The B3PW functional (the 3-parameter hybrid version of PW91) was used in combination with EPR-II[47] basis functions for all light atoms and the triple polarized core properties basis set (CP(PPP)) for copper as implemented in ORCA.

In vivo studies on *Aspergillus niger*

Aspergillus niger NRRL 2270 (A60; ATCC 11414), a well-known citric acid producer strain, was used to test the antioxidant activity of the two complexes. The cultures were grown in 100 mL Erlenmeyer flasks (VWR International Kft., Debrecen, Hungary) containing 20 mL aliquots in a rotary shaker (Infors AG, Basel, Switzerland) operating at 190 RPM and 30° C. The growth medium containing 10 g of D-glucose, 6 g of $NaNO_3$, 1.5 g of KH_2PO_4, 0.5 g of $MgSO_4{\cdot}7H_2O$, and 0.5 g of KCl per liter was supplemented with 20 μL of trace element solution (containing 10 g of EDTA, 4.4 g of $ZnSO_4{\cdot}7H_2O$, 1.01 g of $MnCl_2{\cdot}4{\cdot}H_2O$, 0.32 g of $CoCl_2{\cdot}6H_2O$, 0.315 g of $CuSO_4{\cdot}5H_2O$, 0.22 g of $(NH_4)_6Mo_7O_{24}{\cdot}4H_2O$, 1.47 g of $CaCl_2{\cdot}7H_2O$, and 1.1 g of $FeSO_4{\cdot}7H_2O$ per liter).[48] The pH of the growth medium was set at 6.8 using K_2HPO_4 before the medium was distributed into the flasks and sterilized in an autoclave. The trace element solution and the glucose were supplemented into the medium after sterilization under aseptic conditions. The complete and sterile growth medium was subsequently inoculated in a laminar box with 1.4×106 *A. niger* conidia per mL from a freshly prepared, high-density spore suspension stored in a 0.01% Tween 20 solution. Cultures were regularly inspected using a Zeiss Axio Imager microscope. To increase contrast and visibility, lactophenol cotton blue (Fluca) was added to the samples in a final concentration of 10%.

The mycelial dry cell weight (DCW) of the mycelium was determined by measuring the mycelial mass of each flask at the endpoint of the experiment (90 h). Biomass was collected on a pre-weighed glass wool filter, washed with cold tap water, and dried at 80 °C until constant weight.[49]

The residual concentrations of D-glucose in the growth media were quantified using high-performance liquid chromatography (HPLC; Agilent Technologies 1260 Infinity II, United States). The analysis employed a H^+ exchange column (Bio-Rad Aminex HPX-87H+) at 55 °C, isocratic elution with 10 mM H_2SO_4 as a mobile phase at a flow rate of 0.5 mL min^{-1} and refractive index detection.[50,51]

The cellular uptake of the complexes was determined by measuring the extracellular and intracellular complex concentrations with HPLC, the latter after homogenization (5 min) with a Potter-Elvehjem tissue grinder. Analysis was performed using a KNAUER Azura HPLC equipped with an MWD 2.1L detector. Separation on a Phenomenex Luna C18(2) (5 μm, 250 × 4.6 mm) column was performed using H_2O + 0.1% trifluoroacetic acid and acetonitrile as a mobile phase at a flow rate of 1 mL min^{-1} and UV detection at 230, 254 and 267 nm, respectively.

The experiments performed under oxidative stress conditions utilized twelve 100 mL Erlenmeyer flasks (each containing 20 mL aliquots), arranged in four groups (A–D), each with three replicates. After inoculation, fungal conidiospores were allowed to germinate for 7 hours; selected cultures were then incubated with one of the complexes for the next 31 hours. To induce oxidative stress, *tert*-butyl hydroperoxide (*t*BHP) was added to the cultures at 38 h in 4.56 mM – a concentration that was preliminarily found sufficient to fully induce oxidative stress and reduce cell viability.[52] The treated groups were as follows: A: control (unstressed conditions), B: cells treated with 4.56 mM *t*BHP at 38 hours, C: cells pre-incubated with the copper(II) complex of PyHis (100 μM) and treated with 4.56 mM *t*BHP at 38 hours, and D: cells pre-incubated with the copper(II) complex of PydiHis (100 μM) and treated with 4.56 mM *t*BHP at 38 hours.

Aliquots from these samples (0.4 mL) were collected at 0, 6, 18, 31, 42, 54, 66, 78, and 90 hours and the corresponding glucose concentrations were determined by HPLC. The entire experiment was repeated using five-fold higher concentrations of copper complexes, *i.e.*, 500 μM Cu(II)/PyHis and 500 μM Cu(II)/PydiHis complexes.

Results and discussion

Synthesis

Recently, we have reported the synthetic route to prepare pyridine-2,6-carboxamide-based ligands.[12] Briefly, pyridine-2,6-dicarboxylate was chlorinated in the presence of thionyl chloride to produce *N*,*N*-pyridine-2,6-dicarbonyl chloride almost quantitatively. After removing the excess of thionyl chloride, L-histidine methyl ester dihydrochloride was added to form a carboxamide bond. Hydrolysis of the methyl esters was performed under acidic conditions (Scheme S1). The corresponding ^1H and ^{13}C NMR and MS spectra are provided in the SI (Fig. S1–S6). The copper(II) complexes of the ligands were prepared by mixing equimolar amounts of the ligand and copper(II) chloride solution in water at pH 10.2. The formation of the complexes was confirmed by ESI-MS measurements (Fig. S7 and S8).

Complex formation reactions

The determination of the acid dissociation constants (pK_a) of the ligands is detailed in the SI. The overall stability constants, $\log \beta_{pqr}$, of the Cu(II) complexes were determined by pH-poten-

tiometric titrations and the equilibrium model was corroborated by pH-dependent UV-vis, CD and CW-EPR spectroscopy measurements (Table 1, Tables S2 and S3). In the case of the copper(II)–PyHis system, the experimental data can be fitted well by considering the formation of [Cu(PyHis)], $[Cu(PyHisH_{-1})(H_2O)]^-$ and $[Cu(PyHis)_2]^{2-}$ complexes. The concentration distribution in the Cu(II)–PyHis system at a 1 : 1 metal ion to ligand ratio is shown in Fig. 1a.

PyHis shows high affinity to bind copper(II) and the complex formation starts under acidic conditions. At pH ≈ 2.0, the dominant species is [Cu(PyHis)] and only 20% of the total amount of Cu(II) is present as Cu^{2+}. The UV-vis and CW-EPR spectra confirm that the complex formation process is almost complete at pH 3.0. Based on the anisotropic g and Cu(II) hyperfine parameters (Table S2), the ligand field is estimated to be relatively weak around the copper(II) center.

Presumably, the pyridine moiety and the adjacent carboxylate group form a 5-membered chelate ring with the metal ion including a (N,O) donor set, and the coordination of the imidazole-N leads to the formation of a macrochelate in this complex. The EPR parameters are consistent with the proposed binding mode, and the calculated g_z/A_z value indicates the $d_{x^2-y^2}$ ground state of copper(II) with a square planar or square pyramidal coordination environment (Table 1).[53,54] This implies that at least one water molecule is also present in the primary coordination sphere. Upon increasing the pH, an additional base consumption process leads to the formation of a $[Cu(PyHisH_{-1})(H_2O)]^-$ complex, which is accompanied by characteristic changes in the CD, UV-vis, and CW-EPR spectra (Fig. 2 and S12–S14). The individual spectral components contributing to the CW-EPR spectra are shown in Fig. 3a and S15a.

The noted spectral changes can be explained by the copper(II)-induced ionization and coordination of carboxamide-N. In this complex, copper(II) is accommodated by the (O,3N) donor set, yielding a (5,5,6)-membered joined chelate system. An intense band in the UV-vis spectra at 602 nm is consistent with the binding of three nitrogen atoms and the intense positive Cotton effect at 544 nm together with the negative Cotton effect at 651 nm confirm the coordination of a carboxamide group. The EPR spectra show nitrogen superhyperfine patterns both at room temperature and in frozen solution, allowing an initial estimation of the hyperfine coupling constants between the unpaired electron and the ^{14}N nuclei of the nitrogen atoms directly coordinated to copper(II) (Table S2). However, since the ^{14}N hyperfine couplings were not clearly resolved in all spectra, pulsed EPR measurements were also performed to determine the ^{14}N hyperfine couplings (*vide infra*). Frozen solution CW-EPR spectra can be fitted well by considering the coordination of two equivalent and one non-equivalent nitrogen atoms in the equatorial plane of copper(II) and further support the (N_{py},N^-,N_{Im}) coordination mode. It is noteworthy that the calculated isotropic values, $g_{0,calc}$, based on the principal components of the g-tensors (g_x, g_y, and g_z) are in excellent agreement with those obtained for the solution spectra. This confirms the existence of the same species both in frozen solution and at room temperature. The $[Cu(PyHisH_{-1})(H_2O)]^-$ complex dominates at physiological pH and the formation of mixed hydroxo complexes could not be detected even at high pH. The results of the ESI-TOF-MS measurements confirm the formation of the postulated species. In negative ion mode, the $[Cu(PyHisH_{-1})(H_2O)]^-$ complex is the main ion detected as confirmed by the excellent agreement between the experimental and calculated m/z values (363.9858 *vs.* 363.9863) of the corresponding peak (Fig. S7). Structural and spectroscopic features of the $[Cu(PyHis)_2]^{2-}$ complex are presented in the SI.

Slow evaporation of an aqueous solution of Cu(II)–PyHis system at a 1 : 1 metal ion to ligand ratio and pH 7.0 yields blue crystals of the $[Cu(PyHisH_{-1})(H_2O)]^-$ complex that is suitable for X-ray diffraction measurement. The complex crystallizes in the orthorhombic crystal system in the $P2_12_12_1$ chiral

Table 1 Overall stability constants ($\log \beta_{pqr}$)[a] and selected spectroscopic parameters of the copper(II) complexes formed in the Cu(II)–PyHis and Cu(II)–PydiHis systems

		UV-vis spectroscopy	CD spectroscopy	EPR spectroscopy[b]		
	$\log \beta_{pqr}$	$\lambda_{max}/\varepsilon$ [c]	$\lambda/\Delta\varepsilon$ [c]	g_z	A_z ($\times 10^{-4}$ cm^{-1})	g_z/A_z
Cu(II)–PyHis						
[CuL]	11.67 ± 0.04	618/28	543.5 (+)/0.43 651 (−)/0.17	2.363	151.1	156.4
$[CuLH_{-1}]^-$	9.54 ± 0.04	602/135	543.5 (+)/0.54 651 (−)/0.13	2.219	171.8	129.2
$[CuL_2]^{2-}$	20.17 ± 0.08	602/123	543.5 (+)/0.55 651 (−)/0.13	2.014	122.0	165.1
Cu(II)–PydiHis						
$[CuLH]^+$	14.53 ± 0.06	630/58	557 (+)/0.68 684 (−)/0.05	2.361	147.2	160.4
[CuL]	10.0 ± 0.2	624/106	562 (+)/0.28 684 (−)/0.07	2.225	174.1	127.8
$[CuLH_{-1}]^-$	6.09 ± 0.08	625/98	688 (+)/0.17	2.229	184.6	120.7
$[CuLH_{-2}]^{2-}$	−2.6 ± 0.2	638/189	738 (+)/1.88 624 (−)/0.84	2.213	153.5	144.2

[a] I = 0.2 M KCl, T = 25 °C. [b] The full set of isotropic and anisotropic EPR parameters is given in Table S2. [c] λ in nm, ε or $\Delta\varepsilon$ in M^{-1} cm^{-1}.

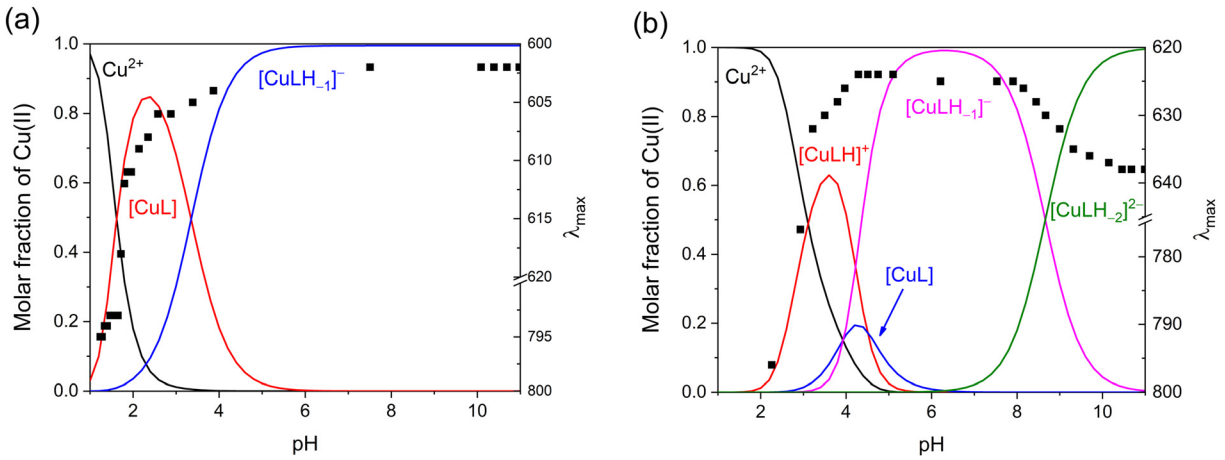

Fig. 1 Distribution of the complexes formed in the Cu(II)–PyHis (a) and Cu(II)–PydiHis (b) systems at a 1 : 1 metal ion to ligand ratio and the λ_{max} value of the d–d band (■) obtained by UV-vis spectroscopy as a function of pH. $c_{Cu(II)}$ = 1.81 mM, c_{PyHis} = 1.90 mM and $c_{PydiHis}$ = 1.90 mM.

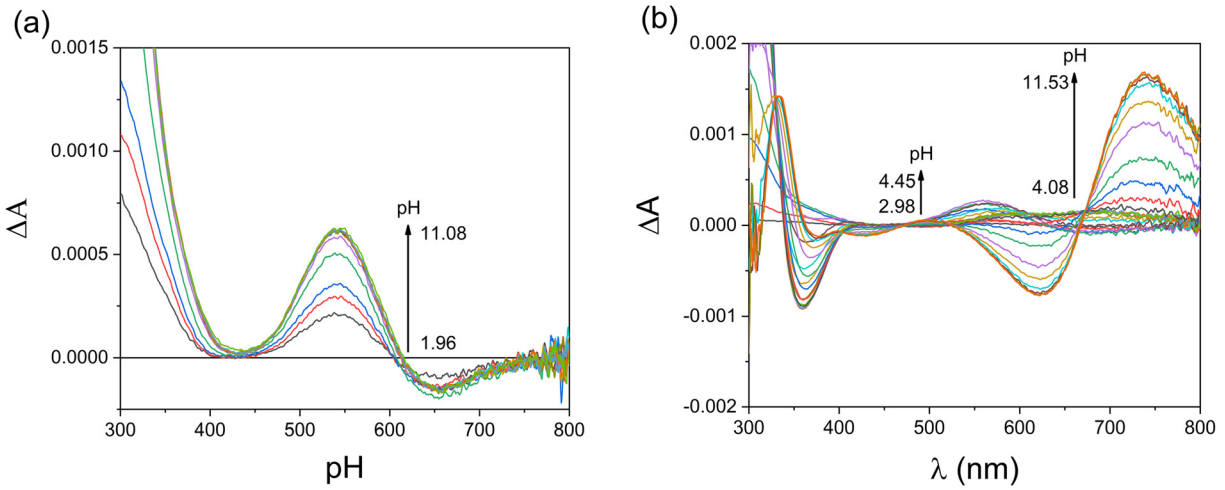

Fig. 2 CD spectra of the Cu(II) : PyHis (a) and PydiHis (b) systems at a 1 : 1 metal ion to ligand concentration ratio as a function of pH. $c_{Cu(II)}$ = 0.95 mM.

space group containing a Na^+ counter ion and six coordinated water molecules. The ORTEP representation of the compound is shown in Fig. 4, and the unit cell is provided in Fig. S17 along with the crystal data collected in Table S4. Selected bond lengths and angles are presented in Table S5. The PyHis ligand coordinates to the copper(II) ion *via* the oxygen atom of the carboxylate group, pyridine-N, carboxamide-N and imidazole-N possessing a (5,5,6)-membered joined chelate system in the equatorial plane of copper(II). The axial positions are accommodated by two solvent water molecules to form an elongated octahedral geometry. The non-coordinating carboxylate group of the ligand is deprotonated, thus the complex exhibits −1 net charge, which is neutralized by a Na^+ ion. These results corroborate the proposed structure of the $[Cu(PyHisH_{-1})(H_2O)]^-$ complex in the solution phase.

The Na^+ ion possesses a rare but precedented square-pyramidal geometry where the oxygen atom of the carboxylate group binds in the apical position and four water molecules are in the equatorial plane.[55]

In the direction of the sixth coordination site (apical position), a pyridine ring of a neighbouring complex is located, which prevents the binding of the sixth water molecule. The water molecules coordinated to the Na^+ ion are not arranged at a regular 90° angle. This is due to the H-bond interactions between the neighbouring complexes. Fig. S18 and S19 show the selected intra- and the main intermolecular H-bond connections in the crystal. Details of the main secondary interactions are presented in Table S6. Fig. S20 shows the packing arrangement viewed from the three crystallographic directions.

In the case of the copper(II)–PydiHis system, the CW-EPR, CD and UV-vis data can be fitted well by considering the formation of four copper(II) complexes. The overall stability constants and selected spectroscopic parameters are presented in

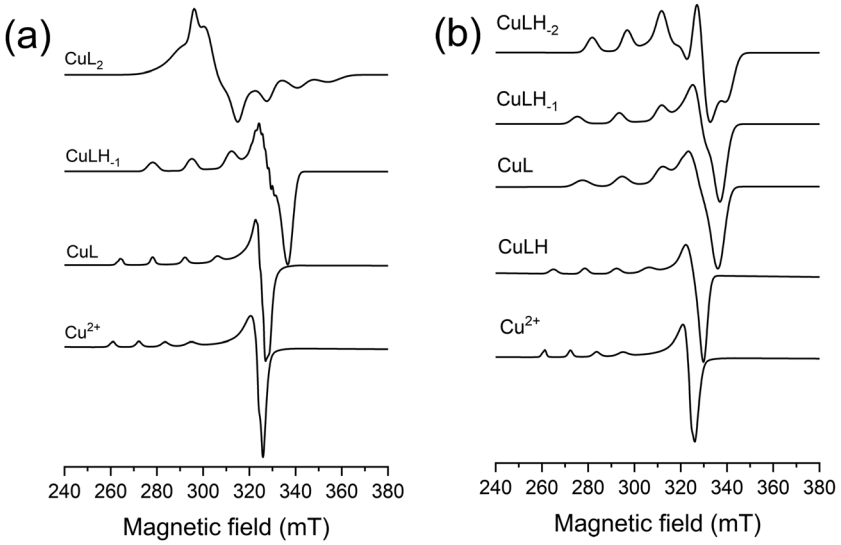

Fig. 3 Calculated component EPR spectra obtained for the Cu(II)–PyHis (a) and Cu(II)–PydiHis (b) complexes based on evaluation of the pH-dependent CW-EPR spectra of the frozen solution (see the SI for simulation of the experimental spectra).

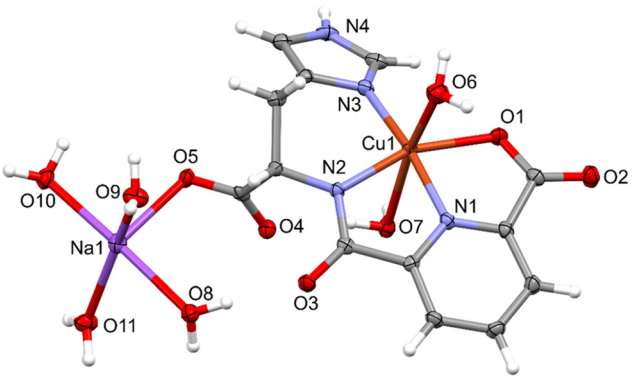

Fig. 4 ORTEP representation of $[Cu(PyHisH_{-1})(H_2O)_2Na(H_2O)_4]$ crystals with atom numbering. Displacement parameters are drawn at the 50% probability level.

Table 1 and the corresponding distribution curves of the complexes are shown in Fig. 1b.

In the case of PydiHis, the complex formation reaction starts only in the slightly acidic pH range with the formation of a $[Cu(H(PydiHis))]^+$ complex. This reaction is accompanied by remarkable changes in the UV-vis spectra (Fig. S21). A significant shift compared to the absorption maxima of the $[Cu(aqua)]^{2+}$ complex (λ_{max} = 800 nm) indicates the binding of nitrogen atoms. According to CD (Fig. 2b) and CW-EPR (Fig. 3b, Table S2) spectroscopy, the ligand field around the copper(II) center is weak, thus we expect the binding of the nitrogen atom of pyridine and macrochelation *via* the imidazole-N of a histidine moiety. This binding mode is further confirmed by the EPR parameters. The anisotropic spin-Hamiltonian parameters of $[Cu(H(PydiHis))]^+$ are similar to those obtained for the [Cu(PyHis)] complex in which copper(II) is coordinated *via* the imidazole-N of histidine and the nitrogen atom of the pyridine residue.

Upon increasing the pH, the binding of the imidazole-N of the second histidine yields the [Cu(PydiHis)] complex, which is present only in a relatively small concentration (Fig. 1b). The binding mode of the ligand is confirmed by the spin Hamiltonian parameters obtained by EPR spectroscopy (Table S2). The [Cu(PydiHis)] complex is suppressed by the formation of $[Cu(PydiHisH_{-1})(H_2O)]^-$, which is the dominant species in the physiological pH range. The CD, UV and CW-EPR spectra exhibit significant changes, confirming the copper(II)-induced ionization and binding of a carboxamide nitrogen (Fig. S15b, S22 and S23). Thus, the coordination sphere of copper(II) is most probably occupied by four N atoms that belong to the pyridine, one carboxamide moiety and two imidazole moieties. ESI-TOF-MS measurement corroborates the formation of this species (Fig. S8). The detected main ion is the $[Cu(PydiHisH_{-1})]^-$ complex and the measured m/z values are in excellent agreement with the calculated values (501.0449 *vs.* 501.0453).

A further base consumption process leads to the formation of a $[Cu(PydiHisH_{-2})]^{2-}$ complex. Although the UV-vis spectra do not exhibit significant changes in this pH range, the CW-EPR spectra clearly show the formation of the new species. In this complex, the second carboxamide-N presumably also coordinates to copper(II), leading to the formation of a (5N) coordinated species. The strong increase of g_y compared to g_x and the change of the copper hyperfine coupling point to a strong admixture of d_{z^2} in the ground state, indicating a significant deviation from a square pyramidal to a distorted trigonal bipyramidal structure.[56] A previous study of distorted 5-coordinated Cu(II) complexes of pyridine-2,6-dicarboxamide

ligands revealed a linear relationship between the copper A_z value and some structural parameters, including basal angles and the degree of distortion between square pyramidal and trigonal bipyramidal geometries (τ parameter).[57] By implementing this result, $[Cu(PydiHisH_{-2})]^{2-}$ is predicted to exhibit basal angles 135° and 160° for N_{py}–Cu–N_{His} and $N_{carboxamide}$–Cu–$N_{carboxamide}$, respectively, which considerably deviate from the 180° expected in a pure square pyramidal structure. This was further confirmed by pulsed EPR spectroscopy (*vide infra*). This complex is prevalent in the alkaline pH range and the compact coordination mode of the ligand prevents the hydrolysis of the copper(II) center.

Superoxide dismutase activity

Since the dismutation of the superoxide anion proceeds *via* the redox cycle between the Cu(I) and Cu(II) oxidation states, cyclic voltammetry was used to determine the Cu(II/I) redox couple. The corresponding cyclic voltammograms are shown in Fig. S24. The redox potentials at pH 7.6 are 0.15 V (*vs.* NHE) for $[Cu(PyHisH_{-1})(H_2O)]^-$ and 0.27 V (*vs.* NHE) for $[Cu(PydiHisH_{-1})(H_2O)]^-$, respectively. These potentials fall within the optimal potential range where the two SOD half reactions occur,[58] thus the complexes are thermodynamically capable of catalyzing the decomposition of the superoxide anion. The catalytic activity of the complexes in the dismutation of the superoxide ion was studied by using the xanthine/xanthine oxidase/NBT assay. The corresponding inhibition curves are shown in Fig. S25 and the estimated IC_{50} values, together with the calculated k_{McCF} and k_{cat} values, (*vide infra*) are presented in Table 2.

At physiological pH, copper(II) exists exclusively in the form of a $[Cu(PyHisH_{-1})(H_2O)]^-$ complex; therefore, the catalytic activity is attributed to this species. In the case of the copper(II)–PydiHis system, most of the copper(II) is present as $[Cu(PydiHisH_{-1})(H_2O)]^-$; however, a minor fraction (approximately 8%) exists as $[Cu(PydiHisH_{-2})]^{2-}$, which may also contribute to the observed SOD activity. Table 2 clearly shows that the copper(II) complexes of PydiHis possess high SOD activity, and the IC_{50} value of this species is two orders of magnitude smaller than that of the PyHis complex. Moreover, the results confirm that the rate constant of the catalytic dismutation of the superoxide anion by the $[Cu(PyHisH_{-1})(H_2O)]^-$ complex (k_{McCF}) is one order of magnitude smaller than the rate constant of the self-dismutation ($k_d = 8.6 \times 10^5$ M^{-1} s^{-1}).[58]

Table 2 IC_{50} values and the kinetic parameters for the superoxide anion dismutation at pH = 7.60. The structures of PydiAla and PydiTyr are shown in Scheme S2

System	IC_{50} (μM)	$k_{McCF}{}^a/10^6$ (M^{-1} s^{-1})	$k_{cat}{}^b/10^6$ (M^{-1} s^{-1})
Cu(II)–PyHis	147 ± 15	0.0182	<0.35
Cu(II)–PydiHis	0.64 ± 0.07	4.2	80 ± 10
Cu(II)–PydiAla[12]	0.35	7.6	n.d.
Cu(II)–PydiTyr[12]	0.028	96.2	n.d.
$Cu(HPO_4)$[59]	0.25	n.d.	n.d.

n.d.: not determined. [a] $k_{McCF} = k_{NBT}[NBT]/IC_{50}$. [b] Obtained by stopped-flow experiments.

The xanthine/xanthine oxidase assay is based on competitive kinetics, and the superoxide anion is always present at a low steady-state concentration level. This implies that only indirect information can be obtained on the SOD activity of the compounds tested, provided that fundamental preconditions are satisfied. Recently, we have demonstrated that dedicated sequential stopped-flow experiments offer insight into the dismutation process under real catalytic conditions.[39] In this study, we performed such experiments by monitoring the decay of the absorbance at 260 nm, which is close to the absorption maximum of the superoxide anion. The corresponding kinetic traces recorded in the copper(II)–PydiHis and copper(II)–PyHis systems at pH 7.6 are shown in Fig. 5 and Fig. S26, respectively. First, the kinetic traces for the spontaneous dismutation of O_2^- were recorded. The rate expression for the decay of O_2^- is given in eqn (1):

$$\frac{d[O_2^-]}{dt} = -k_d[O_2^-]^2 - k_1[O_2^-] \quad (1)$$

where k_d is the second-order rate constant for the spontaneous dismutation and k_1 is the first-order catalytic superoxide decay due to unavoidable impurities in the reactants.[60] Fitting the kinetic traces to the corresponding integrated rate expression (eqn (2)) yields $k_d = (2.9 \pm 0.1) \times 10^4$ M^{-1} s^{-1} and $k_1 = 60 \pm 1$ s^{-1}. Previously, an order of magnitude higher value was reported for k_d on the basis of pulse radiolytic experiments in water.[58] Considering that our experiments were performed in a 1 : 1 aqueous HEPES buffer (50 mM, pH 7.6)/DMSO mixture, the noted difference is attributed to the differences in the applied reaction media.

$$A_t = \frac{A_0 e^{-k_1 t}}{\left(\frac{k_d}{k_1}\right)A_0(1 - e^{-k_1 t}) + 1} + C \quad (2)$$

The kinetic traces shown in Fig. 5 are slightly distorted first-order kinetic curves that can be interpreted by considering the relatively slow spontaneous decomposition and the catalytic dismutation of O_2^-. In addition, the noted effect of the impurities also needs to be considered. It is reasonable to assume that the redox cycling in the dismutation process involves the Cu(I) form in the steady state, thus the reaction is first order in both the Cu(II) form and the superoxide ion. Since the concentration of Cu(II) is practically constant during the overall reaction, the kinetic traces were fitted to the integrated form of the corresponding rate expression (*cf.* eqn (3) and (4)):

$$\frac{d[O_2^-]}{dt} = -k_d[O_2^-]^2 - k'_{cat}[O_2^-] \quad (3)$$

$$A_t = \frac{A_0 e^{-k'_{cat} t}}{\left(\frac{k_d}{k'_{cat}}\right)A_0(1 - e^{-k'_{cat} t}) + 1} + C \quad (4)$$

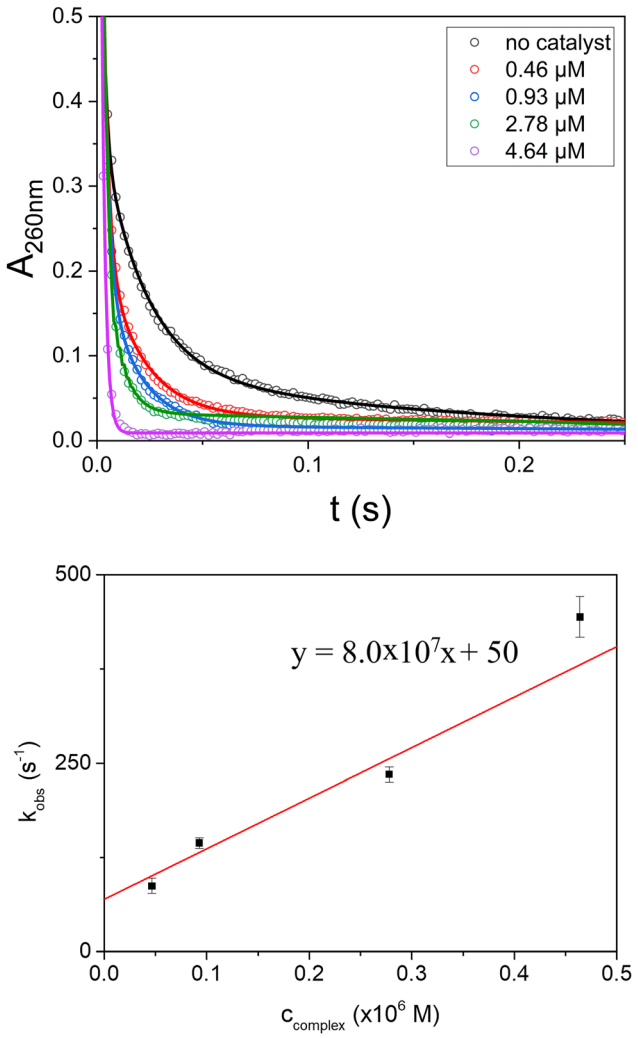

Fig. 5 Top: experimental (markers) and fitted (continuous lines) kinetic traces for the decomposition of the superoxide anion recorded at 260 nm in the absence (black) and presence of the copper(II)–PydiHis complex at pH 7.6 in a 1 : 1 aqueous HEPES buffer (50 mM, pH 7.6)/DMSO mixture. The traces were corrected with the absorbance of the complex for better comparison. The concentration of the catalyst is given in the figure. Experimental data were fitted with eqn (4). Bottom: the dependence of k'_{cat} on the concentration of the copper(II)–PydiHis complex. $c(O_2^{\cdot-})^0$ = 469 μM, λ = 260 nm, T = 25 °C, and l = 0.2 cm.

where A_0 and A_t are the initial and the time-dependent absorbance, respectively. Under the applied conditions, the only absorbing species is $O_2^{\cdot-}$ and the absorbance can be readily converted into the concentration of this species by using the corresponding molar absorptivity, $\varepsilon_{260\ nm}$ = 2686 M^{-1} cm^{-1}. In accordance with the above considerations, k'_{cat} is given in eqn (5):

$$k'_{cat} = k_1 + k_{cat}[complex] \quad (5)$$

The plot of k'_{cat} as a function of the concentration of [Cu(II)] is shown in Fig. 5. The result obtained for k_1 is in excellent agreement with the value obtained on the basis of the spontaneous decomposition of $O_2^{\cdot-}$ (*cf.* eqn (3)).

According to the kinetic experiments, the catalyst is not involved in further degradation processes during the dismutation cycle. This conclusion was corroborated by independent HPLC experiments that did not indicate the formation of a side product (Fig. S27). The second-order rate constants of the copper-catalyzed dismutation of superoxide anion, k_{cat}, are presented in Table 2.

To identify the catalytically active species in the copper(II)–PydiHis system at pH 7.6, the dismutation process was also studied at pH 9.1 (Fig. S28), where $[Cu(PydiHisH_{-2})]^{2-}$ is the dominant species. The lack of any catalytic effect under such conditions clearly demonstrates that this complex is not able to assist the decomposition of the superoxide anion. Therefore, the observed SOD activity at pH 7.6 is attributed to the $[Cu(PydiHisH_{-1})(H_2O)]^-$ complex.

Both the xanthine/xanthine oxidase/NBT assay and the stopped-flow experiments confirm that the $[Cu(PydiHisH_{-1})(H_2O)]^-$ complex shows high SOD activity. In contrast, no detectable catalytic contribution from the $[Cu(PyHisH_{-1})(H_2O)]^-$ complex was observed in the stopped-flow experiments (*cf.* Fig. S26). The xanthine/xanthine oxidase/NBT assay indicated that the latter complex slightly catalyzes the decomposition of the superoxide anion, but this effect can exclusively be observed under the specific experimental conditions of the assay.[38] In this case, due to the low steady-state concentration of the superoxide anion, the second-order spontaneous decomposition becomes negligible, and only the slow complex-catalyzed process is operative.

It needs to be added that there are serious concerns regarding the universal applicability of the xanthine/xanthine oxidase/NBT assay for testing SOD activity and the reliability of the quantitative parameters (IC_{50} and k_{McCF}) obtained by this method.[36,61,62] In this assay, $O_2^{\cdot-}$ is generated in the xanthine/xanthine oxidase reaction and the progress of the process can be monitored by the formation of uric acid, which is a by-product in this system. Independent experiments in the absence of NBT confirmed that the formation of uric acid; therefore the formation of the superoxide anion, is also inhibited by the $[Cu(PyHisH_{-1})(H_2O)]^-$ complex in the xanthine/xanthine oxidase reaction (Fig. S29). Consequently, this effect falsifies the results obtained on SOD activity because the results correspond to the combined effects of two inhibitory reactions. Since the inhibition of the xanthine/xanthine oxidase reaction becomes pronounced at relatively high complex concentrations, it is reasonable to assume that it has a marginal effect on the determination of IC_{50} in the case of highly efficient SOD mimics. The stopped-flow method eliminates this problem and k_{cat} offers a firm basis to establish bias-free SOD activities.

Pulsed EPR and DFT

To gain deeper insights into the differences of the SOD activity of the copper(II) complexes formed at physiological pH, pulsed EPR studies with corroborating DFT computations were carried out. This allowed us to study the structure and intimate spectroscopic features of these species. These studies were completed with the characterization of the copper(II) complex

formed at high pH, $[Cu(PydiHisH_{-2})]^{2-}$, to gain insight into the unusual coordination geometry around the copper(II) center.

The geometry and coordination sphere of $[Cu(PyHisH_{-1})(H_2O)]^-$ are well established by SC-XRD experiments. This species is dominant in the solution phase at pH 7.0, thus the pulsed EPR results obtained in this system under neutral conditions are used as a benchmark for the data recorded in the Cu(II)–PydiHis system at pH 7.0 and 12.0 for which no SC-XRD data are available.

Although the crystal structure of the copper(II) complex of PyHis showed the presence of two coordinated water molecules in axial positions, DFT calculations revealed a pentacoordinate Cu(II) complex with a square pyramidal structure in which the second water molecule was no longer bound to the copper ion. This indicates that the binding of the second water molecule may be induced in the crystal by the packing of the molecule and does not occur in solution (see Fig. S30 for an example of the structure, Tables S7–S9). Although the DFT computations of the EPR parameters of open-shell transition-metal complexes are notoriously difficult and not quantitatively correct at the level of theory used here, they reflect significant trends that can be used to interpret the experimental EPR spectra of the complex in solution. The DFT computations confirm that the largest g value (g_z) and the largest copper hyperfine value (in absolute values, A_z) lie approximately along the $Cu–O_{water}$ axis. In the following discussion, we will refer to the equatorial plane as the plane perpendicular to this axis (g_x, g_y plane).

The ^{14}N HYSCORE spectrum of a frozen solution of Cu(II)–PyHis at pH 7.0 reveals the well-known spectral features of the remote N_ε nucleus of the imidazole ring of a His bound to Cu(II) with the Cu–N bond more or less lying in the equatorial plane (Fig. 6a and Fig. S31, Table S10).[63–66] The DFT computations of $[Cu(PyHisH_{-1})(H_2O)]^-(H_2O)$ confirm this assignment (Table S9). When a similar HYSCORE experiment is set up for a frozen solution of Cu(II)–PydiHis at pH 7.0, similar patterns are observed, but the simulations reveal that all features can be reproduced only when the contributions of two $HisN_\varepsilon$ nuclei are assumed (Fig. 6b and Fig. S32, Table S11). This is clear evidence that the dominant Cu(II)–PydiHis complex at pH 7.0 involves the binding of both His residues.

Davies ENDOR offers an excellent tool to determine the coupling of the unpaired electron with protons and with the copper-bound ^{14}N. Comparison of the Davies ENDOR spectra of Cu(II)–PyHis and Cu(II)–PydiHis at pH 7.0 at a comparable observer position reveals the overall similarities, suggesting that both complexes have an at least partly similar copper ligation pattern (Fig. 6c). In both cases, broad features (marked in orange in Fig. 6c) are observed at frequencies higher than the proton Larmor frequency, ν_H, which confirms strong hyperfine coupling of ^{14}N nuclei (~30–55 MHz). In the case of Cu(II)–PydiHis, the relative intensities of the ^{14}N features *versus* the ^1H peaks are considerably larger than in the case of Cu(II)–PyHis. This is in line with the expected increased number of N-ligands in the former complex. An ENDOR study of Cu(II)-doped L-histidine deuterochloride monodeuterohydrate single crystals found that the copper-bound $HisN_\delta$ nuclei have hyper-

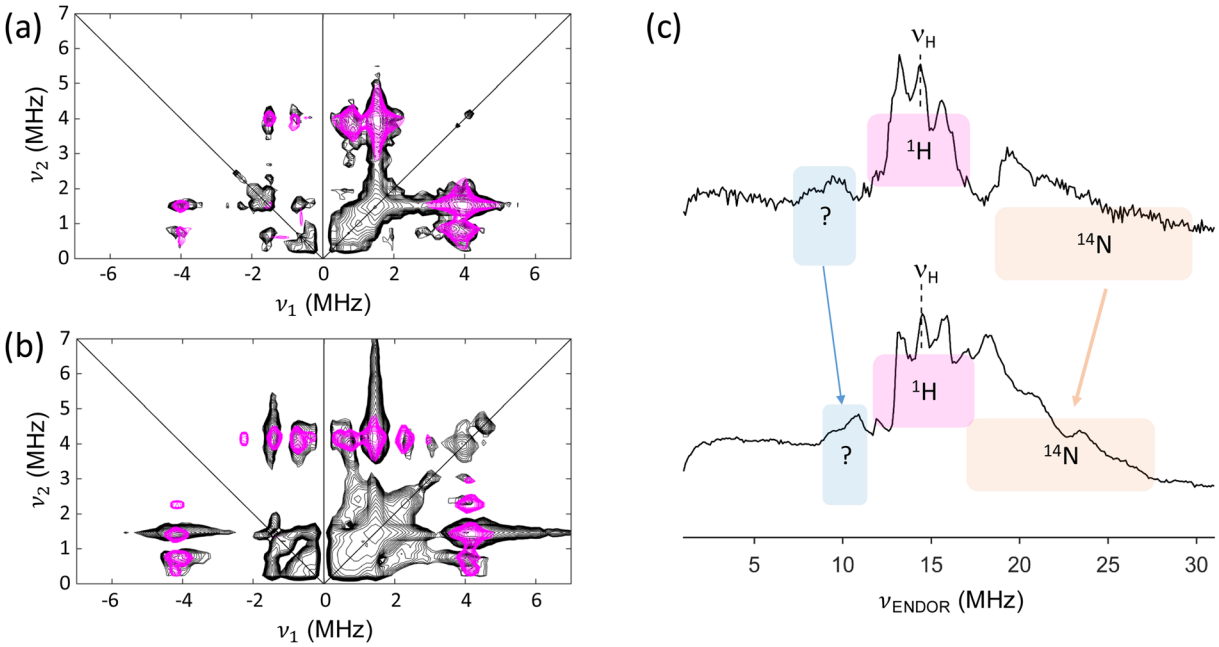

Fig. 6 (Left) Experimental (black) and simulated (magenta) ^{14}N HYSCORE spectra of a frozen solution of (a) Cu(II)–PyHis and (b) Cu(II)–PydiHis at pH 7.0 at observer positions of 337.7 mT and 339.4 mT, respectively. The experimental τ-value is 120 ns. Spectrum (a) was simulated considering the contribution of one ^{14}N nucleus and spectrum (b) was obtained considering two ^{14}N nuclei (see Tables S10 and S11). (Right, c) Comparison of the Davies ENDOR spectra of a frozen solution of (top) Cu(II)–PyHis and (bottom) Cu(II)–PydiHis at pH 7.0 at observer positions of 337.7 mT and 339.4 mT, respectively.

fine values ranging from 27 to 40 MHz, which correspond to ENDOR signals centered at around 13.5–20 MHz (half the hyperfine value).[67] The largest ENDOR signal increase is observed in the 13–25 MHz region (Fig. 6c), matching the contribution of an extra $HisN_{\delta}$. Moreover, the DFT model of Cu(II)–PyHis predicts similar values for the $HisN_{\delta}$, with the amide and pyridine ^{14}N nuclei having larger couplings (Table S10). Indeed, both ENDOR spectra in Fig. 6c show features until ~30 MHz. Furthermore, the ^{14}N ENDOR peaks of Cu(II)–PydiHis are down-shifted as a whole compared to those of Cu(II)–PyHis (see the orange arrow, Fig. 6c), indicating an overall reduction of the spin density on the directly ligated ^{14}N.

In both the ENDOR spectra depicted in Fig. 6c, two distinct peaks can be observed below the proton Larmor frequency (indicated in blue). These features may be due to either ^{1}H or ^{14}N hyperfine interactions. In order to distinguish between these two options, the Mims ENDOR spectra of Cu(II)–PyHis at pH 7.0 were examined (Fig. S33). While Mims ENDOR favors the contributions of the weakly coupled protons, it significantly suppresses the contributions of the strongly coupled ^{14}N nuclei. Furthermore, D_2O exchange experiments reveal that this coupling stems from a non-exchangeable proton (Fig. S33). The features can be satisfyingly simulated at different field positions (Fig. S33), assuming a proton with principal hyperfine values [9.0 13.5 9.0] MHz, similar to the values reported for the proton on the α-carbon of His in Cu(II)–His complexes.[68] This also matches qualitatively the DFT results, which predict this proton to be the only one with a large isotropic hyperfine value (Table S10). In the case of Cu(II)–PydiHis at pH 7.0, this ^{1}H hyperfine coupling decreases somewhat (Fig. S34 and Table S11), in line with the overall decrease observed in the ^{14}N hyperfine values and related spin density.

The above results show that the $[Cu(PydiHisH_{-1})(H_2O)]^{-}$ complex involves the binding of two His residues, and that the binding of the amide nitrogen to copper is retained (observation of the proton at the α-carbon of His). To probe whether axial binding of water to copper occurs, Davies ENDOR experiments were performed in H_2O and D_2O (Fig. S34, right). The subtraction of the spectra reveals the ^{1}H ENDOR features of the exchangeable protons. These can be simulated with ^{1}H hyperfine values (Table S11) in line with the ones predicted by DFT for the $[Cu(PyHisH_{-1})(H_2O)]^{-}(H_2O)$ model (Table S9) and with slightly lower hyperfine anisotropy than those found experimentally for the axial water molecules in $[Cu(H_2O)_6]^{2+}$. This indicates a slightly longer Cu–O bond than for the copper hexaaqua complex.[69]

Detailed pulsed EPR spectroscopic studies on the $[Cu\ (PydiHisH_{-2})]^{2-}$ complex are provided in the SI. These results show that the deprotonation and binding of the second amide nitrogen in PydiHis cause a strong change in the electronic and geometric structure of the complex, with the imidazole residues exhibiting considerable flexibility. This conformational flexibility with a concomitant change of the electronic structure may also occur upon superoxide binding and influence the superoxide dismutase activity. For $[Cu(PyHisH_{-1})(H_2O)]^{-}$, the rigid (5,5,6)-membered joined chelate system is less favorable to accommodate the copper(I) oxidation state during the dismutation process. Our earlier studies confirmed that a slight distortion in the coordination geometry of copper (II) favors such a one-electron reduction process.[12] This distortion and conformational flexibility are operative for the $[Cu(PydiHisH_{-1})(H_2O)]^{-}$ complex. As a result, the binding of the superoxide anion is more favorable for this species, and its distorted structure does not require significant conformational rearrangement during the dismutation process.

In vivo studies

Effect of the copper complexes on fungal growth. To study the antioxidant features of the copper complexes, *Aspergillus niger* was selected as a biological model because it provides a sensitive and well-characterized system to evaluate antioxidant activity. *A. niger* is an obligate aerobe with intense oxygen metabolism and has been shown to generate reactive oxygen species (ROS) under stress conditions, making it a suitable

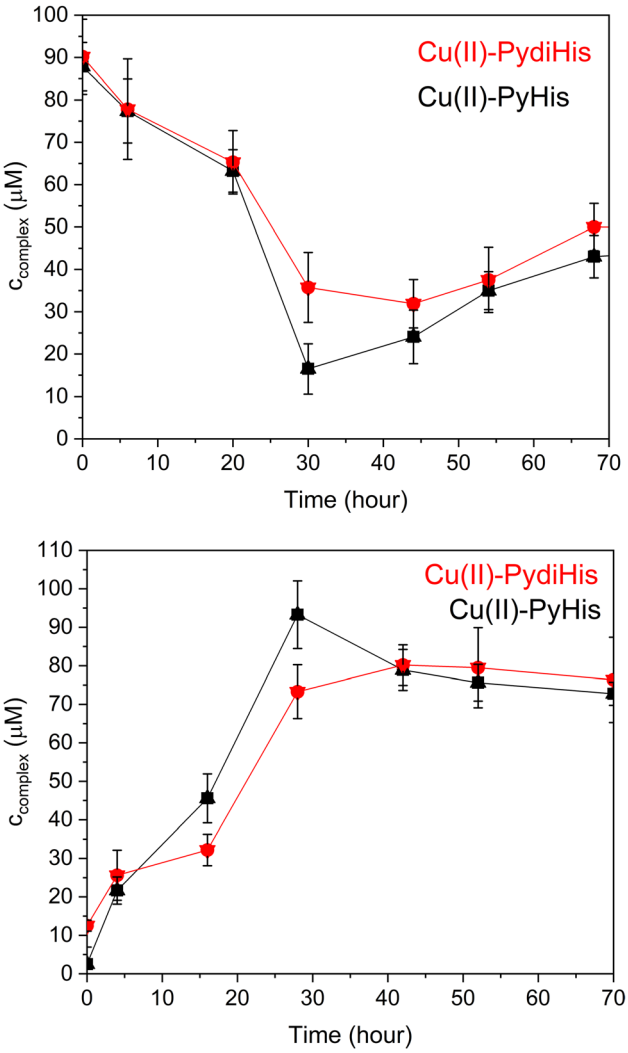

Fig. 7 Kinetic profile of the extracellular (top) and intracellular (bottom) concentrations of the complexes.

organism to monitor oxidative damage and antioxidant protection.[70–72]

Preliminary tests whereby *A. niger* NRRL 2270 cells were exposed to the copper complexes (100 μM) confirmed the absence of intrinsic cytotoxic effects. DCW data implied that the complexes do not inhibit fungal growth relative to the control even after an extended cultivation period (Fig. S41).

Extra- and intracellular complex concentrations. In the first 30 hours of cultivation, the kinetics of the extra- and intracellular concentrations showed a mirror image pattern: while the former values decreased to some 30% (PydiHis) and 25% (PyHis) of the initial values, the latter ones counteracted this by similar increases (Fig. 7). The small, (undetermined) gap in the mass balance of the complexes might be attributed to cell-wall binding, commonly occurring for all sorts of soluble substances in the presence of fungal mycelia. Hence, the majority of the added complexes accumulate intracellularly in the rapid growth phase of the cultivation, followed by secretion back to the growth media. While we cannot explain this latter phenomenon, we note that degradation of fungal cells is becoming visible by this time of the cultivation, likely due to the depletion of glucose – the sole carbon source – from the growth medium. Secretion of the previously accumulated complexes may well be associated with this observation.

Protective effect of the complexes against *tert*-butyl hydroperoxide (*t*BHP)-induced oxidative stress. *tert*-Butyl hydroperoxide (*t*BHP) is a well-established inducer of oxidative stress and has been reported to generate multiple ROS species, including superoxide. Studies have shown that *t*BHP treatment leads to superoxide accumulation.[73–75] As expected, *t*BHP significantly inhibited fungal growth, indicated by diminished glucose uptake and biomass formation (Fig. 8, S42, Tables S16 and S17). However, the presence of complexes significantly enhanced the glucose uptake of mycelia under *t*BHP-induced oxidative stress conditions (C–D) relative to cultures treated with *t*BHP only (B). Hence, the two complexes appear to have an ability to protect (glucose-fuelled) cellular metabolism under oxidative stress.

Of the two complexes, Cu–PydiHis was more effective in terms of mitigating the adverse effect of *t*BHP. As a consequence of increased glucose intake, fungal biomass formation increased as well. Interestingly, Cu–PydiHis not only mitigated the adverse effect of *t*BHP, but stimulated growth beyond control levels. We cannot explain this phenomenon at the moment but note that the extra biomass far exceeds the carbon content of the complex taken up by the cells. Hence, the complexes appear to increase the specific biomass yield (= unit biomass per unit substrate) of *A. niger* on D-glucose.

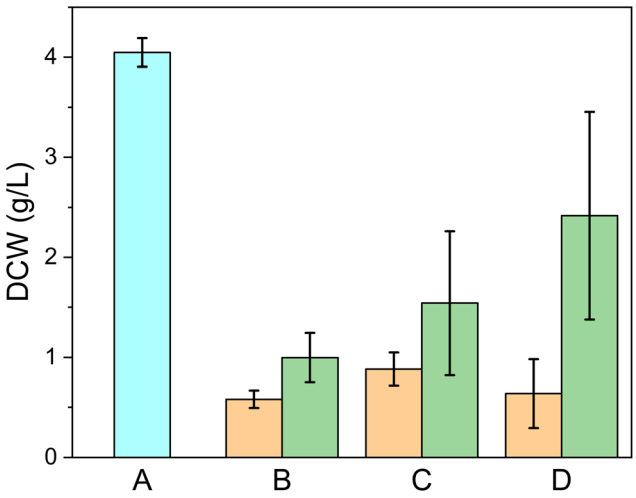

Fig. 8 Fungal biomass (DCW) values (g L^{-1}) at 90 h with standard deviations. The treatment groups were as follows: A: control (unstressed conditions), B: cells treated with 4.56 mM *t*BHP at 38 hours, C: cells pre-incubated with the copper(II) complex of PyHis and treated with 4.56 mM *t*BHP at 38 hours, D: cells pre-incubated with the copper(II) complex of PydiHis and treated with 4.56 mM *t*BHP at 38 hours. Orange: 100 μM complex concentration and green: 500 μM complex concentration.

Conclusions

In this paper, two novel histidine-functionalized pyridine-based ligands, PyHis and PydiHis, were synthesized and their copper(II) complexes were evaluated as superoxide dismutase (SOD) mimics. The structural, thermodynamic, and spectroscopic properties of these complexes were thoroughly characterized.

Although both complexes are thermodynamically capable of decomposing the superoxide anion, only the $[Cu(PydiHisH_{-1})(H_2O)]^-$ complex exhibits significant catalytic efficiency in this process. The superior catalytic activity is attributed to conformational flexibility and favorable coordination geometry, which facilitates superoxide binding and redox cycling. Pulsed EPR and DFT studies corroborate this conclusion.

The xanthine and xanthine oxidase assay (McCord–Fridovich test) and the stopped-flow experiments provide somewhat contradictory results on the SOD activity of the $[Cu(PyHisH_{-1})(H_2O)]^-$ complex. It was confirmed that the complex inhibits the formation of $O_2^{\bullet-}$ in the xanthine/xanthine oxidase reaction, thus falsifying the results obtained by using the assay. Consequently, the McCord–Fridovich assay has limited applicability in this system.

Additionally, *in vivo* assays using *Aspergillus niger* under oxidative stress confirmed the biological efficacy of the complexes. The copper(II) complex of PydiHis not only protected fungal growth under oxidative stress but also enhanced glucose uptake and biomass formation. The exact protective mechanism is not known; it may involve SOD, CAT, or other antioxidant-like activities, which will be the subject of future studies. However, the high activity and biological compatibility of the copper(II) complex of PydiHis may have outstanding prospects in developing novel antioxidants.

Author contributions

The manuscript was written through the contributions of all authors. All authors have given approval to the final version of the manuscript. R. D., A. G., N. Á., I. S., D. Sz., and D. B.-K.: investigation, N. V. M. and E. F.: investigation and formal analysis, L. K.: formal analysis, methodology and writing – original draft, I. F.: funding acquisition and writing – original draft, S. V. D.: investigation, formal analysis, supervision, and writing – original draft, and N. L.: conceptualization, supervision, and writing – original draft.

Conflicts of interest

There are no conflicts to declare.

Data availability

The data supporting this article have been included as part of the supplementary information (SI). Details of the synthesis, NMR and mass spectra of the compound, acid-base equilibria of the ligands, pH-dependent UV-vis and EPR spectra, X-Ray crystallographic data, SOD activity studies and cyclic voltammograms, pulsed EPR and DFT data, details of the *in vivo* studies. See DOI: **https://doi.org/10.1039/d5qi01687h**.

CCDC 2424617 [$Cu(PyHis)(H_2O)_2Na(H_2O)_4$] contains the supplementary crystallographic data for this paper.[76]

Acknowledgements

The authors are grateful for the financial support of the Hungarian National Research, Development and Innovation Office (OTKA K-139140 (I. F.), K-146406 (L. K.) and K-138489 (E. F.)). N. L. acknowledges the financial support of the János Bolyai Research Scholarship of the Hungarian Academy of Sciences and the 2021-4.1.2-NEMZ_KI-2024-00042 project. This work was also supported by the EKÖP-24-3 University Research Scholarship Program of the Ministry for Culture and Innovation from the source of the National Research, Development and Innovation Fund and the University of Debrecen Scientific Research Bridging Fund (DETKA). S. V. D. thanks the Fund for Scientific Research Flanders (FWO-Vlaanderen) for infrastructure funding for the EPR instrumentation (No. I004920N).

References

1 M. Schieber and N. S. Chandel, ROS function in redox signaling and oxidative stress, *Curr. Biol.*, 2014, **24**, R453–R462.
2 J. N. Moloney and T. G. Cotter, ROS signalling in the biology of cancer, *Semin. Cell Dev. Biol.*, 2018, **80**, 50–64.
3 I. A. Abreu and D. E. Cabelli, Superoxide dismutases—a review of the metal-associated mechanistic variations, *Biochim. Biophys. Acta, Proteins Proteomics*, 2010, **1804**, 263–274.
4 A.-F. Miller, Superoxide dismutases: active sites that save, but a protein that kills, *Curr. Opin. Chem. Biol.*, 2004, **8**, 162–168.
5 J. A. Simpson, S. Narita, S. Gieseg, S. Gebicki, J. M. Gebicki and R. T. Dean, Long-lived reactive species on free-radical-damaged proteins, *Biochem. J.*, 1992, **282**, 621–624.
6 C. M. C. Andrés, J. M. Pérez de la Lastra, C. Andrés Juan, F. J. Plou and E. Pérez-Lebeña, Superoxide anion chemistry—Its role at the core of the innate immunity, *Int. J. Mol. Sci.*, 2023, **24**, 1841.
7 A. C. Maritim, R. A. Sanders and J. B. Watkins III, Diabetes, oxidative stress, and antioxidants: A review, *J. Biochem. Mol. Toxicol.*, 2003, **17**, 24–38.
8 H. Wiseman and B. Halliwell, Damage to DNA by reactive oxygen and nitrogen species: Role in inflammatory disease and progression to cancer, *Biochem. J.*, 1996, **313**, 17–29.
9 P. R. Angelova and A. Y. Abramov, Role of mitochondrial ROS in the brain: From physiology to neurodegeneration, *FEBS Lett.*, 2018, **592**, 692–702.
10 C. Policar, J. Bouvet, H. C. Bertrand and N. Delsuc, SOD mimics: From the tool box of the chemists to cellular studies, *Curr. Opin. Chem. Biol.*, 2022, **67**, 102109.
11 S. I. Liochev, Superoxide dismutase mimics, other mimics, antioxidants, prooxidants, and related matters, *Chem. Res. Toxicol.*, 2013, **26**, 1312–1319.
12 R. Diószegi, D. Bonczidai-Kelemen, A. C. Bényei, N. V. May, I. Fábián and N. Lihi, Copper(II) complexes of pyridine-2,6-dicarboxamide ligands with high SOD activity, *Inorg. Chem.*, 2022, **61**, 2319–2332.
13 I. Batinic-Haberle, Z. Rajic, A. Tovmasyan, J. S. Reboucas, X. Ye, K. W. Leong, M. W. Dewhirst, Z. Vujaskovic, L. Benov and I. Spasojevic, Diverse functions of cationic Mn(III) N-substituted pyridylporphyrins, recognized as SOD mimics, *Free Radicals Biol. Med.*, 2011, **51**, 1035–1053.
14 H. Y. V. Ching, I. Kenkel, N. Delsuc, E. Mathieu, I. Ivanović-Burmazović and C. Policar, Bioinspired superoxide-dismutase mimics: The effects of functionalization with cationic polyarginine peptides, *J. Inorg. Biochem.*, 2016, **160**, 172–179.
15 M. Stojičkov, S. Sturm, B. Čobeljić, A. Pevec, M. Jevtović, A. Scheitler, D. Radanović, L. Senft, I. Turel, K. Andjelković, M. Miehlich, K. Meyer and I. Ivanović-Burmazović, Cobalt(II), zinc(II), iron(III), and copper(II) complexes bearing positively charged quaternary ammonium functionalities: Synthesis, characterization, electrochemical behavior, and SOD activity, *Eur. J. Inorg. Chem.*, 2020, **2020**, 3347–3358.
16 H. Kurosaki, R. K. Sharma, S. Aoki, T. Inoue, Y. Okamoto, Y. Sugiura, M. Doi, T. Ishida, M. Otsuka and M. Goto, Synthesis, characterization, and spectroscopic properties of three novel pentadentate copper(II) complexes related to the metal-chelating inhibitors against DNA binding with

HIV-EP1, *J. Chem. Soc., Dalton Trans.*, 2001, 441–447, DOI: 10.1039/B006949N.
17 F. Turtaut, S. Ouahrani-Bettache, J.-L. Montero, S. Köhler and J.-Y. Winum, Synthesis and biological evaluation of a new class of anti-brucella compounds targeting histidinol dehydrogenase: α-O-arylketones and α-S-arylketones derived from histidine, *MedChemComm*, 2011, **2**, 995–1000.
18 G. Gran, Determination of the equivalence point in potentiometric titrations. Part II, *Analyst*, 1952, **77**, 661–670.
19 H. M. Irving, M. G. Miles and L. D. Pettit, A study of some problems in determining the stoicheiometric proton dissociation constants of complexes by potentiometric titrations using a glass electrode, *Anal. Chim. Acta*, 1967, **38**, 475–488.
20 I. Nagypál and L. Zékány, Computational methods for the determination of formation constants, in *Computational Methods for the Determination of Stability Constants*, ed. D. Leggett, Plenum Press, New York, 1985, pp. 291–299.
21 Hydra/Medusa Chemical Equilibrium Database and plotting software, K. R. I. o. T., 2004 https://www.kemi.kth.se/medusa/.
22 A. Rockenbauer, T. Szabó-Plánka, Z. Árkosi and L. Korecz, A two-dimensional (magnetic field and concentration) electron paramagnetic resonance method for analysis of multispecies complex equilibrium systems. Information content of EPR spectra, *J. Am. Chem. Soc.*, 2001, **123**, 7646–7654.
23 A. Rockenbauer and L. Korecz, Automatic computer simulations of ESR spectra, *Appl. Magn. Reson.*, 1996, **10**, 29–43.
24 P. Höfer, A. Grupp, H. Nebenführ and M. Mehring, Hyperfine sublevel correlation (hyscore) spectroscopy: A 2D ESR investigation of the squaric acid radical, *Chem. Phys. Lett.*, 1986, **132**, 279–282.
25 W. B. Mims, Pulsed endor experiments, *Proc. R. Soc. London, Ser. A*, 1965, **283**, 452–457.
26 E. R. Davies, A new pulse endor technique, *Phys. Lett. A*, 1974, **47**, 1–2.
27 S. Stoll and A. Schweiger, EasySpin, a comprehensive software package for spectral simulation and analysis in EPR, *J. Magn. Reson.*, 2006, **178**, 42–55.
28 T. Higashi, *NUMABS – Numerical Absorption Correction*, Rigaku Corporation, Tokyo, Japan, 1999.
29 CrystalClear SM 1.4.0 Rigaku/MSC Inc.
30 M. C. Burla, R. Caliandro, B. Carrozzini, G. L. Cascarano, C. Cuocci, C. Giacovazzo, M. Mallamo, A. Mazzone and G. Polidori, Crystal structure determination and refinement via SIR2014, *J. Appl. Crystallogr.*, 2015, **48**, 306–309.
31 G. Sheldrick, Crystal structure refinement with SHELXL, *Acta Crystallogr., Sect. C: Struct. Chem.*, 2015, **71**, 3–8.
32 L. Farrugia, WinGX and ORTEP for Windows: An update, *J. Appl. Crystallogr.*, 2012, **45**, 849–854.
33 A. Spek, Single-crystal structure validation with the program PLATON, *J. Appl. Crystallogr.*, 2003, **36**, 7–13.
34 C. F. Macrae, P. R. Edgington, P. McCabe, E. Pidcock, G. P. Shields, R. Taylor, M. Towler and J. van de Streek, Mercury: Visualization and analysis of crystal structures, *J. Appl. Crystallogr.*, 2006, **39**, 453–457.
35 F. H. Allen, O. Johnson, G. P. Shields, B. R. Smith and M. Towler, CIF applications. XV. enCIFer: A program for viewing, editing and visualizing CIFs, *J. Appl. Crystallogr.*, 2004, **37**, 335–338.
36 W. F. Beyer and I. Fridovich, Assaying for superoxide dismutase activity: Some large consequences of minor changes in conditions, *Anal. Biochem.*, 1987, **161**, 559–566.
37 S. Durot, C. Policar, F. Cisnetti, F. Lambert, J.-P. Renault, G. Pelosi, G. Blain, H. Korri-Youssoufi and J.-P. Mahy, Series of Mn complexes based on N-centered ligands and superoxide – reactivity in an anhydrous medium and SOD-like activity in an aqueous medium correlated to MnII/MnIII redox potentials, *Eur. J. Inorg. Chem.*, 2005, **2005**, 3513–3523.
38 R. F. Pasternack and B. Halliwell, Superoxide dismutase activities of an iron porphyrin and other iron complexes, *J. Am. Chem. Soc.*, 1979, **101**, 1026–1031.
39 D. Bonczidai-Kelemen, G. Sciortino, N. V. May, E. Garribba, I. Fábián and N. Lihi, Introducing the penicillamine moiety into a metallopeptide mimicking the NiSOD enzyme: electronic and kinetic effects, *Inorg. Chem. Front.*, 2022, **9**, 310–322.
40 M. S. I. Microcal, *2018 OriginPro 2018b*, Northampton, MA.
41 F. Neese, The ORCA program system, *Wiley Interdiscip. Rev.: Comput. Mol. Sci.*, 2012, **2**, 73–78.
42 F. Neese, Software update: The ORCA program system—Version 5.0, *Wiley Interdiscip. Rev.: Comput. Mol. Sci.*, 2022, **12**, e1606.
43 J. P. Perdew, Density-functional approximation for the correlation energy of the inhomogeneous electron gas, *Phys. Rev. B: Condens. Matter Mater. Phys.*, 1986, **33**, 8822–8824.
44 J. P. Perdew, Erratum: Density-functional approximation for the correlation energy of the inhomogeneous electron gas, *Phys. Rev. B: Condens. Matter Mater. Phys.*, 1986, **34**, 7406–7406.
45 A. D. Becke, Density-functional exchange-energy approximation with correct asymptotic behavior, *Phys. Rev. A*, 1988, **38**, 3098–3100.
46 A. Schäfer, H. Horn and R. Ahlrichs, Fully optimized contracted Gaussian basis sets for atoms Li to Kr, *J. Chem. Phys.*, 1992, **97**, 2571–2577.
47 V. Barone, in *Recent Advances in Density Functional Methods*, 1995, pp. 287–334. DOI: 10.1142/9789812830586_0008.
48 E. Fekete, V. Bíró, A. Márton, I. Bakondi-Kovács, Z. Németh, E. Sándor, B. Kovács, I. Fábián, C. P. Kubicek, A. Tsang and L. Karaffa, Bioreactor as the root cause of the "manganese effect" during *Aspergillus niger* citric acid fermentations, *Front. Bioeng. Biotechnol.*, 2022, **10**, 935902.
49 J. Kozma and L. Karaffa, Effect of oxygen on the respiratory system and cephalosporin-C production in *Acremonium chrysogenum*, *J. Biotechnol.*, 1996, **48**, 59–66.
50 B. Fejes, J.-P. Ouedraogo, E. Fekete, E. Sándor, M. Flipphi, Á. Soós, Á. P. Molnár, B. Kovács, C. P. Kubicek, A. Tsang and L. Karaffa, The effects of external Mn^{2+} concentration

on hyphal morphology and citric acid production are mediated primarily by the NRAMP-family transporter DmtA in *Aspergillus niger*, *Microb. Cell Fact.*, 2020, **19**, 17.

51 L. Karaffa, E. Sándor, J. Kozma and A. Szentirmai, Methionine enhances sugar consumption, fragmentation, vacuolation and cephalosporin-C production in *Acremonium chrysogenum*, *Process Biochem.*, 1997, **32**, 495–499.

52 L. Karaffa, K. Váczy, E. Sándor, S. Biró, A. Szentirmai and I. Pócsi, Cyanide-resistant alternative respiration is strictly correlated to intracellular peroxide levels in *Acremonium chrysogenum*, *Free Radical Res.*, 2001, **34**, 405–416.

53 S. Gama, F. Mendes, F. Marques, I. C. Santos, M. F. Carvalho, I. Correia, J. C. Pessoa, I. Santos and A. Paulo, Copper(II) complexes with tridentate pyrazole-based ligands: synthesis, characterization, DNA cleavage activity and cytotoxicity, *J. Inorg. Biochem.*, 2011, **105**, 637–644.

54 S. Bunda, N. V. May, D. Bonczidai-Kelemen, A. Udvardy, H. Y. V. Ching, K. Nys, M. Samanipour, S. Van Doorslaer, F. Joó and N. Lihi, Copper(II) complexes of sulfonated salan ligands: Thermodynamic and spectroscopic features and applications for catalysis of the Henry reaction, *Inorg. Chem.*, 2021, **60**, 11259–11272.

55 C. Chen, C. Sommer, H. Thisgaard, V. McKee and C. J. McKenzie, Facile transmetallation of $[SbIII(DOTA)]^-$ renders it unsuitable for medical applications, *RSC Adv.*, 2022, **12**, 5772–5781.

56 M. Q. Ehsan, Y. Ohba, S. Yamauchi and M. Iwaizumi, EPR and ENDOR study of trigonal bipyramidal copper complexes with a nitrogen donor tripodal ligand, *Bull. Chem. Soc. Jpn.*, 2006, **69**, 2201–2209.

57 D. S. Marlin, M. M. Olmstead and P. K. Mascharak, Structure–spectroscopy correlation in distorted five-coordinate Cu(II) complexes: A case study with a set of closely related copper complexes of pyridine-2,6-dicarboxamide ligands, *Inorg. Chem.*, 2001, **40**, 7003–7008.

58 D. T. Sawyer and J. S. Valentine, How super is superoxide?, *Acc. Chem. Res.*, 1981, **14**, 393–400.

59 G. Csire, S. Timári, J. Asztalos, J. M. Király, M. Kiss and K. Várnagy, Coordination, redox properties and SOD activity of Cu(II) complexes of multihistidine peptides, *J. Inorg. Biochem.*, 2017, **177**, 198–210.

60 B. J. Bolann, H. Henriksen and R. J. Ulvik, Decay kinetics of $O_2^{\cdot-}$ studied by direct spectrophotometry. Interaction with catalytic and non-catalytic substances, *Biochim. Biophys. Acta, Gen. Subj.*, 1992, **1156**, 27–33.

61 E. E. Kelley, N. K. H. Khoo, N. J. Hundley, U. Z. Malik, B. A. Freeman and M. M. Tarpey, Hydrogen peroxide is the major oxidant product of xanthine oxidase, *Free Radicals Biol. Med.*, 2010, **48**, 493–498.

62 A. V. Peskin and C. C. Winterbourn, Assay of superoxide dismutase activity in a plate assay using WST-1, *Free Radicals Biol. Med.*, 2017, **103**, 188–191.

63 S. Van Doorslaer, G. M. Cereghetti, R. Glockshuber and A. Schweiger, Unraveling the Cu^{2+} binding sites in the C-terminal domain of the murine prion protein: A pulse EPR and ENDOR study, *J. Phys. Chem. B*, 2001, **105**, 1631–1639.

64 Q. Lam, C. Van Stappen, Y. Lu and S. A. Dikanov, HYSCORE and QM/MM studies of second sphere variants of the Type 1 copper site in azurin: Influence of mutations on the hyperfine couplings of remote nitrogens, *J. Phys. Chem. B*, 2024, **128**, 3350–3359.

65 P. M. Schosseler, B. Wehrli and A. Schweiger, Complexation of copper(II) with carbonate ligands in aqueous solution: A CW and Pulse EPR study, *Inorg. Chem.*, 1997, **36**, 4490–4499.

66 J. Haak, O. Golten, M. Sørlie, V. G. H. Eijsink and G. E. Cutsail, pH-mediated manipulation of the histidine brace in LPMOs and generation of a tri-anionic variant, investigated by EPR, ENDOR, ESEEM and HYSCORE spectroscopy, *Chem. Sci.*, 2025, **16**, 233–254.

67 C. A. McDowell, A. Naito, D. L. Sastry, Y. U. Cui, K. Sha and S. X. Yu, Ligand endor study of Cu(II)-doped l-histidine deuterochloride monodeuterohydrate single crystals at 4.2 K, *J. Mol. Struct.*, 1989, **195**, 361–381.

68 M. J. Colaneri and J. Peisach, An electron spin-echo envelope modulation study of copper(II)-doped single crystals of L-histidine hydrochloride monohydrate, *J. Am. Chem. Soc.*, 1992, **114**, 5335–5341.

69 N. M. Atherton and A. J. Horsewill, Proton ENDOR of Cu $(H_2O)_6^{2+}$ in $Mg(NH_4)_2(SO_2)_4.6H_2O$, *Mol. Phys.*, 1979, **37**, 1349–1361.

70 M. Kreiner, L. M. Harvey and B. McNeil, Oxidative stress response of a recombinant *Aspergillus niger* to exogenous menadione and H_2O_2 addition, *Enzyme Microb. Technol.*, 2002, **30**, 346–353.

71 M. Breitenbach, M. Weber, M. Rinnerthaler, T. Karl and L. Breitenbach-Koller, Oxidative stress in fungi: Its function in signal transduction, interaction with plant hosts, and lignocellulose degradation, *Biomolecules*, 2015, **5**, 318–342.

72 H. Simaan, S. Lev and B. A. Horwitz, Oxidant-sensing pathways in the responses of fungal pathogens to chemical stress signals, *Front. Microbiol.*, 2019, **10**, 567.

73 N. Masood, S. Anjum and S. Ahmed, Inactivation of Ras1 in fission yeast aggravates the oxidative stress response induced by tert butyl hydroperoxide (tBHP), *Mol. Biol.*, 2023, **57**, 692–699.

74 C. Wu, W. Zhao, J. Yu, S. Li, L. Lin and X. Chen, Induction of ferroptosis and mitochondrial dysfunction by oxidative stress in PC12 cells, *Sci. Rep.*, 2018, **8**, 574.

75 X. Jiang, M. Li, Y. Wang, C. Wang, Y. Wang, T. Shen, L. Shen, X. Liu, Y. Wang and X. Li, 1,2,4,5-Tetrazine-tethered probes for fluorogenically imaging superoxide in live cells with ultrahigh specificity, *Nat. Commun.*, 2023, **14**, 1401.

76 CCDC 2424617: Experimental Crystal Structure Determination, 2025, DOI: **10.5517/ccdc.csd.cc2md0gj**.